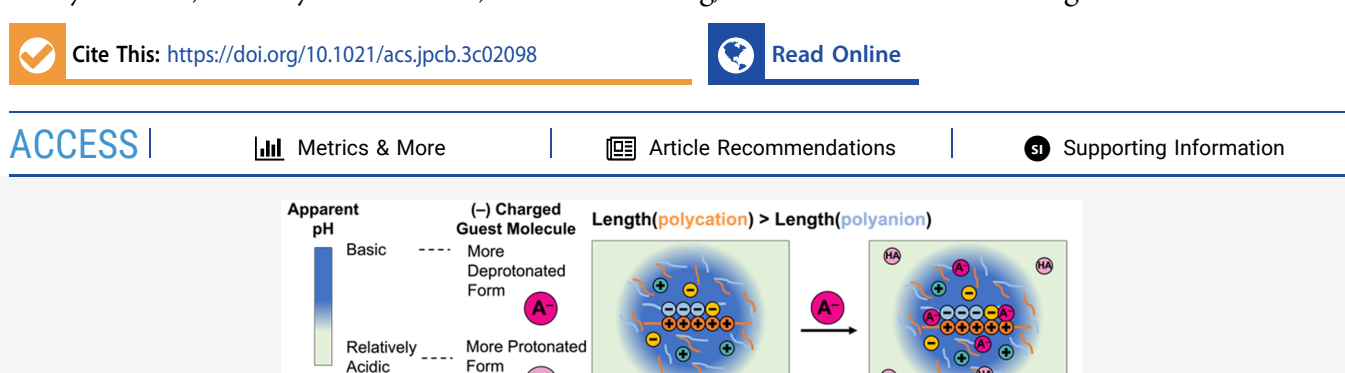


pubs.acs.org/JPCB Article

Effect of Polypeptide Complex Coacervate Microenvironment on Protonation of a Guest Molecule

Saehyun Choi, Ashley R. Knoerdel, Charles E. Sing, and Christine D. Keating

HA



ABSTRACT: Complex coacervate droplets formed by the liquid—liquid phase separation of polyelectrolyte solutions capture several important features of membraneless organelles including their ability to accumulate guest molecules and to provide distinct microenvironments. Here, we examine how polyions in complex coacervates can influence localized guest molecules, leading to a shifted protonation state of the guest molecule in response to its electrostatic environment. A fluorescent ratiometric pH indicator dye was used as a model guest molecule able to report its protonation state in the coacervate phase. Experimentally observed differences in dye-reported local apparent pH inside versus outside of coacervate droplets were largest for polyion pairs having lower salt stabilities and/or larger polyion length mismatch, which we attribute to the relative concentration of open sites on polyions within the coacervates based on theoretical calculations. Using the transfer matrix method, we confirmed that theoretical phase diagrams and critical salt stabilities generated for each polyion pair were consistent with experimental turbidity measurements and estimated the amount of available binding sites on polyions for guest molecules. We conclude that dye molecules likely experience an effective pK_a shift due to interactions with coacervate polyions rather than reporting directly on local proton concentrations. Such a local pK_a shift can also be anticipated for other guest molecules having protonatable groups, including, for example, many metabolites, ligands, and/or drug molecules that partition into coacervates or membraneless organelles based on ion pairing interactions.

■ INTRODUCTION

Complex coacervates formed by oppositely charged aqueous (bio)polymers undergoing liquid-liquid phase separation provide a different chemical and physical microenvironment from the continuous dilute phase due to their much higher polymer concentration. 1-4 Partitioning of guest molecules into the polyelectrolyte-rich coacervate phase enables coacervate droplets to function as microcompartments and is important to their use as models for intracellular membraneless organelles.^{2,3} The droplet and continuous phases have different media effects that can include viscosity, solvent polarity, and availability of interactions with molecular components of the phase such as the abundant polymer species in the coacervate phase.^{2,3} Many types of guest molecules have been accumulated in coacervates, including organic dyes,^{5,6} small molecule cofactors and metabolites, 7-9 nucleic acids, 10-14 and proteins. 15-17 In some cases, changes in guest molecule structure and/or function due to encapsulation within coacervates have been reported; for example, RNAs exhibit different ribozyme kinetics, folding, and duplex dissociation thermodynamics depending on the composition of their coacervate microenvironments. ^{10,12,13,18,19} Coacervate microenvironments are sensitive to their molecular composition, which in turn depends on the identity, charge density, and length of the polyelectrolytes as well as the ionic strength of the solution. ^{7,11,12} How to leverage this tunability of coacervate microenvironments to control the chemical state and function of accumulated guest molecules is not yet well understood.

molecules enriched near polyelectrolyte complexes

In general, a higher charge density and greater number of charged monomeric units (length) per polyelectrolyte provide more distinct phase compositions and hence can be expected to provide more distinct microenvironments. For example, the total polyelectrolyte content in coacervate phase increases with

Received: March 29, 2023 Revised: June 5, 2023



increasing polyelectrolyte length. 20,21 Most studies are performed using either matched polyelectrolyte lengths (same number of monomeric repeats) or uncontrolled lengths. Although few systematic studies of length-asymmetric polyelectrolyte systems have been performed, coacervate rheological properties and phase diagrams appear to be dominated by the shorter polymers. 22,23 In prior studies of length-dependent compartmentalization by coacervates formed from oppositely charged homopeptides, we found that local apparent pH inside versus outside coacervate droplets differed by as much as ~0.5 pH units. This was done using the ratiometric pH indicator dye, 5-(and 6)-carboxy SNARF-1 (SNARF), which has dual fluorescence emission peaks that change depending on the dye's protonation state and is commonly used to determine local pH in microenvironments where direct pH measurements are impossible or impractical (e.g., intracellularly).²⁴ Within our small sample size of six peptide-based coacervate systems, the difference in local apparent pH inside vs outside was largest for mismatched polypeptide lengths (SI Figure 5d in ref 12).

Changes in indicator pK_a due to the local microenvironment are not uncommon and often cannot be readily distinguished from changes in local pH.^{25,26} Recent studies have shown polyelectrolytes in solution by themselves can modulate local apparent pH in bulk solution when polyelectrolytes are covalently attached to enzymes allowing enzymatic reactions at otherwise unfavorable pH.²⁷⁻³⁰ The side chains of weak acid/weak base polyelectrolytes exhibit pK_a shifts due to complexation.^{31–33} For example, recent work from Schlenoff and co-workers, ³¹ in qualitative agreement with theory by Knoerdel et al.,³⁴ reports pK_a shifts of up to 3.6 pH units for synthetic polyelectrolytes in solid complexes. Microenvironments in proteins, e.g., in enzyme active sites, can also induce substantial p K_a changes of amino acids. 35,36 Polyelectrolyte gels exhibit similar behaviors, altering the local apparent pH by coupling to local molecular interactions.³⁷ Within complex coacervates, the locally high concentration of charged groups of polyelectrolytes can be expected to influence the interactions among molecules, potentially altering proton and/or ion distribution around them, influencing protonation states. Changes in either the true pH or the p K_a of guest molecules are both potentially significant microenvironmental effects that could alter the chemistry of guest molecules present in a membraneless compartment, such as a complex coacervate or intracellular biocondensate. Decoupling these effects of local electrostatics influencing apparent pH and/or pK_a of molecules in coacervates is challenging experimentally; however, it is feasible in theory and computer simulations.

Coarse-grained^{21,38-41} and atomistic simulations,⁴² along

Coarse-grained^{21,38–41} and atomistic simulations,⁴² along with theoretical polymer physics,^{42,43} can provide useful insights that help interpret experimental coacervation results. A wide variety of approaches have been used to model polymer complexation, such as polymer field theory,^{21,44–50} scaling arguments,^{51–56} liquid state theories,^{57–59} ion pairing models,^{60–65} and coarse-grained simulation.^{21,38,40,54} These models build on classic Voorn–Overbeek theory,^{20,66,67} which captures the essential competition between mixing entropy (via the Flory–Huggins theory of polymer mixing⁶⁸) and electrostatic attraction (via the Debye–Hückel free energy of charge interactions^{69,70}). However, we require a method that accurately models this physical competition in coacervation and resolves the local electrostatic environment around a polyelectrolyte charge that governs the "apparent pH". We use

a recently developed the transfer matrix model of complex coacervation because it specifically considers the local pairing between ions in coacervate forming systems and thus captures a local electrostatic environment while also providing phase diagram predictions. This theory is successful at modeling coacervate phase behavior, including how it is affected by several molecular features, such as multivalent ions, sequence-defined polyelectrolytes and polyampholytes, that is affected polyelectrolytes, crowding due to neutral polymers, and the self-assembly of coacervate-forming block copolyelectrolytes.

Here, we experimentally and theoretically demonstrate how interactions between a guest molecule and polyion binding sites within complex coacervates can shift the protonation state of the guest molecule in a coacervate-dependent manner. Experimental model systems of coacervates composed of polylysine (polyK) and polyaspartate (polyD) with a range of lengths including symmetric and asymmetric polyion lengths were chosen due to their chemical simplicity and their chemical similarity to phase separating proteins in cells. 12 A transfer matrix approach was employed to generate phase diagrams and predict changes in the protonation state for a small anionic guest molecule. This approach allowed us to evaluate the impact of varying the length of polycationic and polyanionic species on the availability of cationic binding sites for the guest molecule. Experimentally, the use of a fluorescent ratiometric pH indicator (SNARF) as the guest molecule provided a means to determine its protonation state inside the coacervates. Results from theory and experiment showed good agreement for the impact of different polyion length pairings on the phase behavior and guest protonation state. Theoretical calculations demonstrated this relationship further by testing various sizes and charges of guest molecules. This work provides a mechanistic understanding for the observed changes in apparent local pH within coacervate droplets and points to scenarios where the effect of electrostatic interactions between guest molecules and the component polyions can be expected to have the largest impact on guest protonation states (or other charge equilibria). Coacervate microenvironment-mediated changes in guest molecules are of interest for controlling reactivity in artificial cells and can be expected to play a role in the biochemistry of intracellular membraneless organelles.

METHODS

Chemicals and Sample Preparation. Poly(L-lysine hydrochloride) (PolyK, Kn, degree of polymerization n = 10and 30 (K10 and K30, respectively)) and poly(L-aspartic acid sodium salt) (PolyD, Dm, degree of polymerization m = 5, 10, 30, and 100 (D5, D10, D30, and D100, respectively)) were purchased from Alamanda Polymers and were used without further purification. Peptide stock solutions were prepared by dissolving them in HPLC water followed by pH adjustment to pH 8.2 \pm 0.1 by 1 M NaOH with peptide concentrations from 50 to 300 mM in monomeric concentrations depending on the lengths of polypeptides. The ratiometric pH indicator dye 5-(and 6)-carboxy SNARF-1 (C-SNARF-1 or SNARF, CAS No. 126208-12-6) was purchased from ThermoFisher Scientific and dissolved in HPLC water to 2.5 mM. Aliquots of SNARF stock solution were mixed with coacervate samples to be 25 μM in final concentration. The coacervate with S0NARF samples was prepared by mixing stock solutions in this order allowing a homogeneous partitioning of SNARF in coacervate droplets: water, salt buffers, Tris buffer (pH 8.1 \pm 0.1 of 10

mM in final concentration), polyD (10 mM in monomeric concentration), SNARF, and polyK (10 mM in monomeric concentration). Samples with "no added salt" contain only the salts coming as counterions for polypeptides, while low and high salt samples have an additional 15 mM KCl or 150 mM KCl with 0.5 mM MgCl₂ in final concentration, respectively.

Turbidity Measurement. 100 μ L of coacervate samples in each salt concentration was prepared in each well of a Corning 96 well special optics plate. Absorbance spectra for each well were recorded from 300 to 1000 nm using a Tecan M1000 Pro microplate reader. The UV-vis absorbance value at 500 nm is used to calculate turbidity of coacervate samples using the formula turbidity (%) = $10^{(2-Abs_{500\ nm,coacervate}+Abs_{500\ nm,saltbuffer})}$. The turbidity fitting method is based on the method described in previous work. 12 Turbidity curves as a function of KCl concentration were fit to the modified Hill equation (eq 6), using weighted fitting by IgorPro Ver. 6.37 software. The fitting parameter $S_{1/2}$ is the concentration of K⁺ at the half-year maximum that states the transition salt concentration of coacervate formation (Table S1). The fitting parameter $T_{\rm max}$ indicates the maximum turbidity at 0 mM KCl, which was determined from the fit. The fitted value of n ranged from 4.7 to 17.6 according to the steepness of the curve. In deriving eq 6, the minimum value of the turbidity was set to zero, which is consistent with all of the data.

$$T = T_{\text{max}} \left[\frac{1}{([K^+]/S_{1/2})^n + 1} \right]$$
 (6)

Local Apparent pH Measurement. Local apparent pH measurement was performed as described in our previous work. 12 For the calibration curves, emission spectra of SNARF from 560 to 700 nm in various pH solutions were measured by a Jobin Yvon Horiba FL3-21 fluorometer with 5 nm slit size, 5 average scan, and 543 nm excitation. The pH of calibration solution was adjusted by addition of NaOH or HCl solutions and measured by a Mettler Toledo Ultra Micro ISM electrode (micro pH probe). For coacervate samples, we measured the SNARF emission curves in coacervate droplets in/out by lambda scan using an Olympus Fluoroview 1000 confocal microscope simultaneously (Figure S1). Excitation was provided by a 543 nm laser with varied intensity and gain to prevent saturation of the SNARF emission: 35-50% laser intensity and 500-600 V gain. An RP 20/80 filter was utilized. The lambda scan was collected with a 5 nm step size and 10 nm bandwidth. Ten ROIs per image were collected to estimate the local apparent pH of coacervate droplets from three or more independent samples. We then measured the pH of supernatant phase by a micro pH probe after 2 h of equilibration and 15 min of centrifugation. We validated the calibration by comparing the dilute phase pH by electrode to the estimated apparent pH of dilute phase by confocal microscopy (Figure S2). We performed control experiments showing Tris buffer, MgCl₂, or initial pH of samples does not alter the local apparent pH trends in Figures S3-S5.

Theoretical Models for Polyelectrolyte Liquid—Liquid Phase Separation. We model polyelectrolyte coacervation in the pH range where both polyelectrolytes are fully charged by using the transfer matrix model. The transfer matrix approach accounts for charge correlations in polyelectrolyte solutions via "ion pairing" or polymer connectivity arguments.⁷¹ This is motivated by simulation models, which exhibit pair correlation functions with features that are primarily governed by spatially

adjacent neighbors.³⁸ We account for the high salt and polymer concentrations necessary for coacervation by mapping the complicated three-dimensional structure of a coacervate system into a simplified adsorption model shown in Figure 1a.^{41,71,72} The test polyelectrolyte chain is treated as a series of

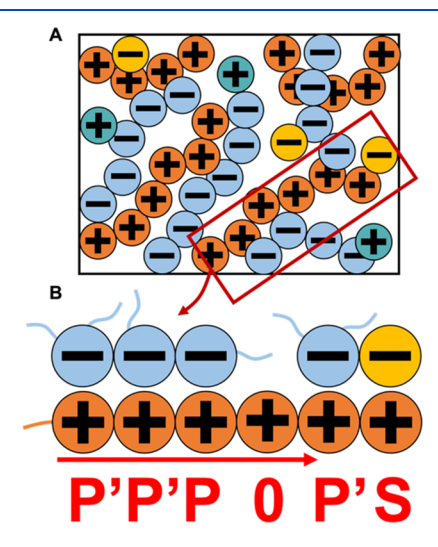


Figure 1. Schematic describing the transfer matrix model of polyelectrolyte coacervates. (A) Coacervate-forming polyelectrolyte solution consisting of polycations (orange), polyanions (blue), cations (teal), and anions (yellow). In the transfer matrix model we consider test polymers, such as the boxed polycation, which are mapped to a one-dimensional adsorption model shown in panel (B). In this representation, the adsorption sites can have states denoted as S, P, P', or 0. The transfer matrix formalism systematically builds up the partition function on a monomer-by-monomer basis (indicated by the red arrow), accounting for the contributions of each possible state to a single-chain interaction free energy.

adsorption sites that can adsorb oppositely charged species. Each adsorption site can enter into one of four states depending on whether the adsorbed species is the oppositely charged salt ion (S), polyelectrolyte (P or P'), or if the site is vacant (0). Figure 1b illustrates these four states as well as the difference between the initial adsorbed polyelectrolyte charge (P') and subsequent sequentially adsorbed polyelectrolyte charges (P). We denote the state of adsorption site i as $s_i = \{S, P, P', 0\}$.

We define the transfer matrix as the Boltzmann factors associated with the energetic contributions from pairs of adjacent monomer sites with states s_{i+1} and s_i (eq 1).

$$M_{s_{i+1}s_i} = \begin{bmatrix} SS & SP & SP' & SO \\ PS & PP & PP' & PO \\ P'S & P'P & P'P' & P'O \\ OS & OP & OP' & OO \end{bmatrix} = \begin{bmatrix} A_- & A_- & A_- & A_- \\ 0 & E_- & 2E_- & 0 \\ B_- & B_- & B_- & B_- \\ D & D & D & D \end{bmatrix}$$

The first form of the matrix depicts the pairs of states for each matrix element with the i+1 state, followed by the i state. We define $A_{-}=\exp(\beta\mu_{S_{-}})=A_{0}\phi_{S_{-}}, B_{-}=\exp(\beta\mu_{P_{-}})=B_{0}\phi_{P_{-}}$, and $D=\exp(-\epsilon)\approx 1$. The last term is dependent on ϵ , which is the energetic penalty incurred when site i+1 is unpaired and thus has an adsorption state of 0. The A_{-} and B_{-} are exponential factors related to the salt and polymer species chemical potentials, respectively. They carry a subscript "—" to denote that these terms apply to the species adsorbing to the

test chain polycation chain are negatively charged. The E_{-} term is written as $E_{-} = (N_{\rm P} - 2)/N_{\rm P}$, which deviates from the value $E_{-} = 1$ used in our prior work 34,71 to account for the probability of reaching the end of the adsorbed polyanion chain; this is non-negligible when we consider short adsorbing chains.

Using the grand canonical ensemble and $M_{s_{i+1}s_i}$ as defined above, we can demonstrate that the partition function for a polycation of length $N_{\rm P}$, $\Xi_{\rm int,+}(N_{\rm P})$, used to describe this adsorption model is in eq 2.

$$\Xi_{\text{int},+}(N_{\text{P}}) = \sum_{s_{N}} \sum_{s_{N-1}} \sum_{s_{N-2}} \sum_{s_{N-3}} M_{s_{N},s_{N-1}} M_{s_{N-1},s_{N-2}} M_{s_{N-2},s_{N-3}} \Xi_{\text{int},+}(1|s_{1})$$
(2

 $\Xi_{\text{int,+}}(1|s_1)$ is the partition function for the end of the polycation test chain which is given by the vector (eq 3).

$$\Xi_{\text{int},+}(1|s_1) = \vec{\Psi}_0 = [A_{-}, 0, B_{-}, D]^T$$
 (3)

We can write the recursive partition function equation more compactly using $\vec{\Psi}_0$ and $\vec{\Psi}_1^T = [1,1,1,1]$ to give eq 4.

$$\Xi_{\text{int},+}(N_{\text{p}}) = \vec{\Psi}_{1}^{\text{T}} M^{N_{\text{p}+}} \vec{\Psi}_{0} \tag{4}$$

Here, $M^{N_{\rm P+}}$ indicates the $N_{\rm P+}$ multiplication of matrix ${\bf M}$, reflecting the degree of polymerization of the polyelectrolyte. The transfer matrix formalism used to define $\Xi_{\rm int,+}(N_{\rm P})$ accounts for the interaction of a test chain with the adsorbing species of opposite charge. We can incorporate this into the overall free energy density for a coacervate-forming solution of polyelectrolytes (eq 5).

$$\begin{split} &\frac{\mathcal{F}}{Vk_{\rm B}T} = \frac{\phi_{\rm P+}}{N_{\rm P+}} \ln \phi_{\rm P+} + \frac{\phi_{\rm P-}}{N_{\rm P-}} \ln \phi_{\rm P-} + \sum_{\alpha=\rm W,+,-} \phi_{\alpha} \ln \phi_{\alpha} \\ &- \frac{\phi_{\rm P+}}{2N_{\rm P+}} \ln \Xi_{\rm int,+} - \frac{\phi_{\rm P-}}{2N_{\rm P-}} \ln \Xi_{\rm int,-} \\ &+ \zeta \left[\Lambda(\phi_{\rm P+} + \phi_{\rm P-}) + \sum_{\alpha=+,-} \phi_{\alpha} \right]^{3} \\ &+ \zeta_{\rm es} [\phi_{\rm P+} - \phi_{\rm P-} + \phi_{\rm S+} - \phi_{\rm S-}]^{2} + \chi \phi_{\rm W}(\phi_{\rm P+} + \phi_{\rm P-}) \end{split}$$

The first three terms account for the configurational entropy of mixing, and the next two terms are the interaction free energies as determined by transfer matrix theory. The subsequent terms (terms six and seven) depict the charged particle hard-sphere packing penalty and an electroneutrality constraint, respectively. The final term consists of a χ contribution to account for the polyelectrolyte solvophobicity.

This free energy expression accounts for two-body pairwise interactions via both the transfer matrix calculations and the χ contributions to the free energy. While the transfer matrix calculations account for some local correlations that represent higher-order charged interactions, we also include a phenomenological cubic term to represent the higher-order excluded volume repulsions between charged species. This excluded volume term accounts for the packing free energy at high volume fractions, which is significant for coacervates where the volume of solute species can be as high as 10-30%. The electroneutrality term is needed to maintain electroneutrality in our Monte Carlo (MC) scheme (described later) and penalizes systems that deviate from electroneutrality in each

phase. We use a large constant $\zeta_{es} = 50.0$ to strongly penalize these deviations. We calculated the phase boundaries in this model by starting the calculation with two identical system compositions. We then move a random amount of each species (anion, cation, polyanion, polycation, or water) from one system to the other, maintaining the initial composition of the two systems combined. The new free energy density for each box is calculated and compared to the previous system free energy $\Delta F = F_{\text{new}} - F_{\text{old}}$. The new systems are either accepted or rejected based on the Metropolis criterion, $p_{\text{ACC}} = \min[1,$ $\exp(-\beta \Delta F)$]. This MC-based scheme has the advantage of efficiently evaluating phase behavior in multicomponent systems, but deviations in the location of the phase boundaries can occur due to the stochastic nature of these calculations. This is addressed in part by including a prefactor to the free energy $\Delta F \rightarrow C_0 \Delta F$, where C_0 is increased until the minimum free energy state is found.

For this paper, we perform these calculations with a variety of parameters; we vary the lengths of the polyelectrolytes by keeping the polyanion length at one of two values ($N_{\rm P}-=10,30$) and varying the polycation length $N_{\rm P+}=5,7,10,30,100$ to represent the various lengths of the polyK and polyD polypeptides considered in experiment. We use several parameters established in our prior work, ³⁴ assuming that the positive and negative polyelectrolyte parameters are equivalent: $A_0=41.0,\,B_0=24.4,\,\zeta=19.0,$ and A=0.6875.

Local Apparent pH Calculation Using Computational Models. We use transfer matrix theory to predict the observed apparent pH difference, ΔpH_a , between the supernatant and coacervate phases of a coacervate-forming system. The ΔpH_a reflects the local change in the equilibrium charge state of dye molecules used to measure pH in the two phases; in experiment, this dye is SNARF-1, but for geometric parameters in the theory we will occasionally use values associated with rhodamine B, a dye molecule in the same family. To understand how the charge state of the dye molecules is affected by the coacervate environment, we consider the physical system in Figure 2. The dye is modeled as having two different off-chain charge states: A, which has a charge of $z_{\rm Dye}$ = -2, and B, which has a charge of $z_{\rm Dye}$ = -3 with an energy of equilibrium associated with charge states A and B defined as

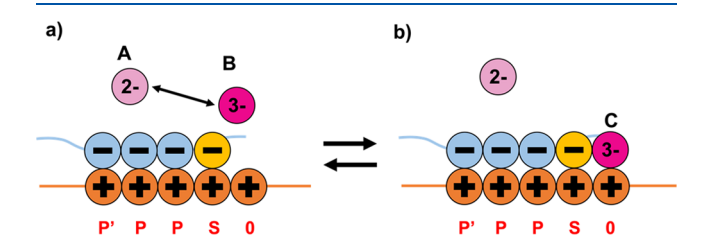


Figure 2. Schematic illustrating our model for SNARF protonation—deprotonation and apparent pH in the presence of coacervate-forming polyelectrolytes. Our three-state model considers that the dye molecule (pink) exists in a pH-dependent equilibrium between different protonation states away from the polyelectrolytes (a, between states A and B). The two states exhibit different fluorescence spectra, which is the typical behavior of this dye when it is used to report pH. However, in a coacervate the dye can adsorb to a polyelectrolyte monomer in state S or 0 (b, state C) where it remains in the highly charged state due to the favorable electrostatic interactions with the polyelectrolyte species. This adsorption affects the equilibrium of the two protonation states, which is observed as a shift in the effective pH.

A PolyK (n = 10, 30) (m = a + b = 5, 10, 30, 100)
$$* - \begin{bmatrix} H & CH - C & O \\ CH_2 & CH_2 & CH_2 \\ CH_2 & CH_2 & CH_2 \end{bmatrix}$$

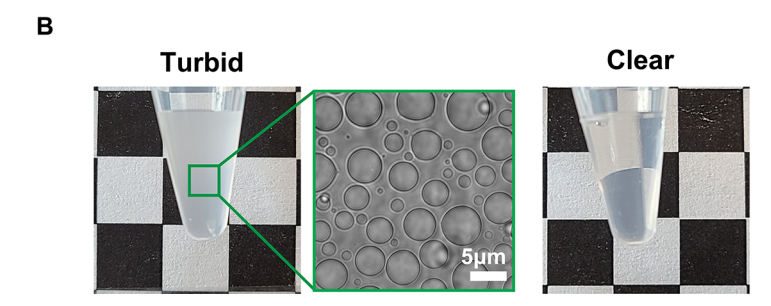


Figure 3. Model polypeptide system and coacervate characterization. (A) In experiments, we form complex coacervates from a series of poly(L-lysine) (polyK) and poly(L-aspartic acid) (polyD), with n and m monomeric units, respectively. Specific chains and lengths are written as Kn and Dm in our notation, and visual representations will model monomers of polyK and polyD as orange and blue circles, respectively. (B) Coacervate formation is characterized by turbidity, which is also apparent visually; the turbid solution on the left is forming a coacervate, which is seen in corresponding micrographs that show the coacervate droplets, and the solution on the right is transparent and thus a single miscible phase. Images correspond to the samples of 1 mM K10 and 1 mM D10 in 10 mM Tris (pH 8.2) and in 15 mM KCl with 0.5 mM MgCl₂ (left, turbid) or 600 mM KCl with 0.5 mM MgCl₂ (right, clear). Black and white squares $(0.5 \times 0.5 \text{ cm}^2)$ at the backgrounds are used to ease the visual comparison of the turbidity of solution.

 ΔE_0 . We also consider there to be a single "ion-paired" state C, which has a charge of $z_{\rm Dye}$ = -3. We assume that there is a significant electrostatic benefit of being in this highly charged state next to the oppositely charged chain, precluding the possibility of an $z_{\rm Dye}$ = -2 state on the chain. The equilibrium among A, B, and C in Figure 2 is affected by the local charge environment in the coacervate and supernatant phases, namely, the likelihood of the dye adsorbing to the polymer chain altering the probability that the dye is in the $z_{\rm Dye}$ = -2 versus $z_{\rm Dye} = -3$ charge states. To model how the coacervate versus supernatant environments affect this equilibrium, we treat the dye as a sixth component to the system but one that does not affect the coacervate phase equilibrium. Upon determining this equilibrium state, we consider that the dye can adsorb to the test chain in the sites unoccupied by the adsorbed polymer or salt. This means that if the state of an adsorption site is 0, a dye molecule can be adsorbed, and a dye molecule cannot be adsorbed if the state of the site is S, P, or P'. The volume available to the unabsorbed dye is defined by the volume

$$\phi_{\rm u} = 1 - \left(1 - \frac{\phi_{\rm P-}}{N_{\rm P+}} \frac{\partial \ln \Xi_{\rm int,P+}}{\partial \phi_{\rm P-}} - \frac{\phi_{\rm L}}{N_{\rm P+}} \frac{\partial \ln \Xi_{\rm int,P+}}{\partial \phi_{\rm L}}\right) \phi_{\rm P+}$$
(7)

Here, the second term is the product of the fraction of unoccupied sites on the polyelectrolyte chain (in parentheses) and the volume fraction of the chain itself. We subtract from one because we want to determine the volume of everything *except* the unoccupied sites, which is where the dye would adsorb. For our results, we use $\Xi_{\text{int},P+}$ for the lowest salt

concentration for each system, corresponding to the salt condition where the most phase separation occurs. The system depicted in Figure 2 also has an energy of interaction term that describes the pairing interaction between the dye and the adsorption site. This is an attractive Coulombic energy contribution, ϵ_1 , that depends on the interaction distance between the center of the dye molecule and the center of the adsorption site. We describe the distance of interaction, $\sigma_{\rm int}$ by eq 8.

$$\sigma_{\rm int} = \sigma_{P+} + \sigma_{\rm Dye} \tag{8}$$

The attractive ion pairing energy, ϵ_1 , is given by

$$\epsilon_{1} = \frac{z_{\text{Dye}} z_{\text{P}+} e^{2}}{4\pi \epsilon_{0} \epsilon_{\text{W}} \sigma_{\text{int}}} \tag{9}$$

Here, $z_{\rm Dye}$ is the charge valency of the dye in state C, $z_{\rm P+}$ is the charge valency of the adsorption site, e^2 is the elementary charge, ϵ_0 is the permittivity of free space, and W is the dielectric constant of the solvent. In our system, we use the dielectric constant of water for the solvent, $\epsilon_{\rm W} = 78.5$, and use bulk densities to estimate the interaction length scales $\sigma_{\rm Dye} = 9.11$ Å and $\sigma_{\rm P+} = 5.26$ Å. We use $\phi_{\rm u}$ and ϵ_1 to calculate the ratio between the amount of dye in charge states B, $f_{\rm B}$, and C, $f_{\rm C}$, to the amount of dye in charge state A, $f_{\rm A}$, in the coacervate phase. This ratio is given by eq 10.

$$\left[\frac{f_{\rm B} + f_{\rm C}}{f_{\rm A}}\right]_{\rm coac} = \frac{\phi_{\rm u} + (1 - \phi_{\rm u})e^{-3\beta\epsilon_{\rm l}}}{\phi_{\rm u}}e^{-\Delta E_{\rm 0}}$$
(10)

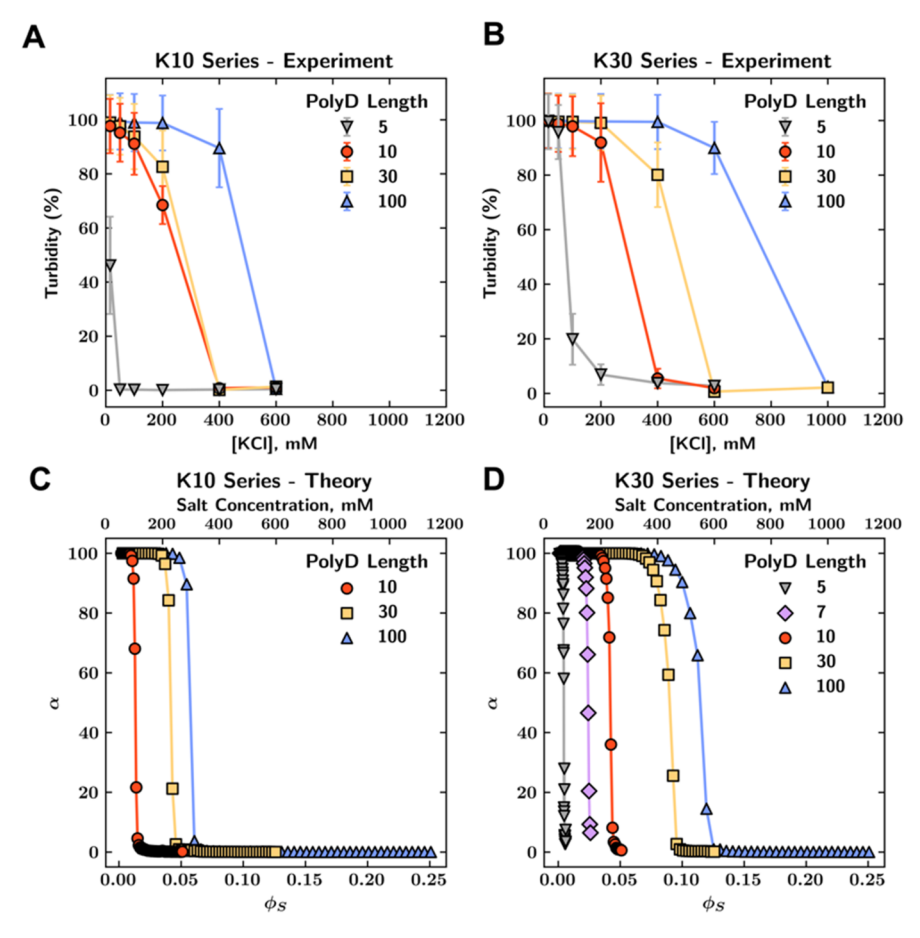


Figure 4. Comparison of experiments and theoretical calculations for complex coacervation behavior as a function of salt concentration. (A) and (B) quantify this turbidity over several lengths of polyK and polyD as a function of salt concentration. Adapted with permission from ref 12. Copyright 2020 Springer Nature. K10/D30, K10/D100, K30/D10, and K30/D100 are newly included here. In general, phase separation is no longer observed (i.e., turbidity is 0%) above a salt resistance $S_{1/2}$, and this occurs at an increasing salt concentration as polyD and/or polyK increases in length. (C) and (D) show this same trend using the transfer matrix theory, which shows similar values of $S_{1/2}$ as in the experiment for the quantity α which serves as a proxy for turbidity in our model and is a function of the difference in water concentration $\Delta \phi_W$ in the coacervate versus supernatant phases.

The factor of 3 in the state C Boltzmann factor $e^{-3\beta\epsilon_1}$ corresponds to the three adsorption sites that can bind to dye of valency $z_{\rm Dye}=-3$. ΔE_0 accounts for the energy difference between the B and C states and the A states, which is related to the bare equilibrium constant between the -2 and -3 charged states. Using this, we more simply define the ratio between $f_{\rm B}$ and $f_{\rm A}$ in the supernatant phase to be eq 11.

$$\left[\frac{f_{\rm B}}{f_{\rm A}}\right]_{\rm sup} = e^{-\Delta E_0} \tag{11}$$

We use the preceding two equations to calculate the ΔpH_a using eqs 12 and 13.

$$\Delta p H_{a} = -\ln \left(\frac{\left[\frac{f_{B} + f_{C}}{f_{A}} \right]_{coac} e^{-\beta E_{c}}}{\left[\frac{f_{B}}{f_{A}} \right]_{sup}} \right)$$
(12)

$$\Delta p H_{a} = -\ln \left(\frac{\phi_{u} + (1 - \phi_{u}) e^{-2\beta \epsilon_{1}}}{\phi_{u}} e^{-\beta E_{c}} \right)$$
(13)

 ΔE_0 is present in both the coacervate and supernatant equations; therefore, the result does not depend on its value. The addition of $\mathrm{e}^{-\beta E_e}$ is a phenomenological term that shifts the graph vertically and may be attributed to dielectric or solubility differences between the two phases not taken into account in this minimalist model. We keep this parameter constant at $\beta E_e = 1.65$ for all conditions we consider. Using the methods described in this section, we investigated the effects of mismatched chain lengths on coacervation.

■ RESULTS AND DISCUSSION

Phase Diagram of Length Mismatch Polyelectrolyte Coacervation. We first characterize the polypeptide systems that we will use in this paper to relate the experimental observations and theoretical predictions of phase behavior and provide context for understanding the local electrostatic environment within the coacervate droplets. Figure 3a shows our experimental system, a set of polylysine (polyK)/polyaspartate (polyD) polypeptide pairs with varying polyK and polyD lengths (denoted as Kn and Dm, where n and m are the degrees of polymerization for each polypeptide). The ability to form a coacervate phase is experimentally determined by turbidity measurements and optical microscopy, as shown in Figure 3b, which compares a turbid coacervate suspension,

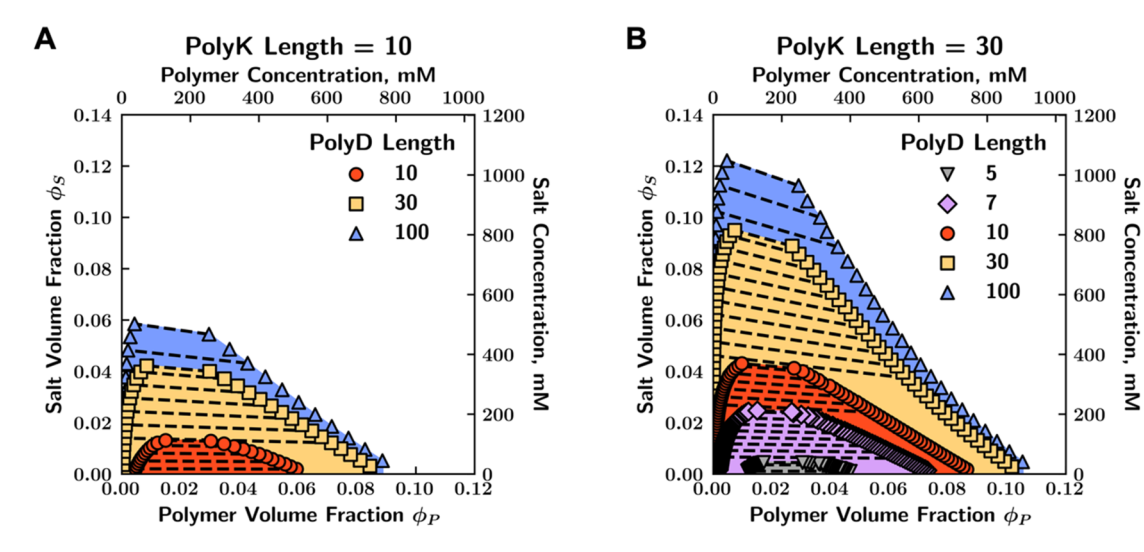


Figure 5. Theoretical phase diagrams for polypeptide coacervates. The full phase diagram, on the salt volume fraction ϕ_S versus polymer volume fraction ϕ_P plane, for K10 (A) and K30 (B) for several polyD lengths each. Both volume fractions and corresponding salt concentrations are plotted, allowing us to make predictions for the polymer concentration in the coacervate phase for use in modeling the apparent pH. Representative tie lines are denoted, illustrating the partitioning of salt in each phase.

where microscale coacervate droplets scatter light to make the solution cloudy (left images), with a clear peptide solution that has not undergone phase separation (right image). Complex coacervation is sensitive to the solution ionic strength. Figures 4a and 4b plot the turbidity of Kn + Dm solutions with several chain lengths as a function of increasing solution ionic strength (as added KCl). In Figures 4a and 4b, K10 and K30, respectively, are combined with D5, D10, D30, and D100. These measurements are performed at a fixed polymer concentration (10 mM in monomeric concentration for each PolyK and PolyD) and a stoichiometric 1:1 K:D monomer ratio, where the extent of coacervation is expected to be maximum. These turbidity measurements were used to quantify the salt concentration where turbidity is at 50% from the parameter from turbidity curves fitting $(S_{1/2}, Table S1)$, which is obtained from eq 6 in Figures 4a,b and is a useful proxy for the strength of coacervation. Salt resistance increases with the lengths of *Kn* and *Dm* chains, consistent with previous experimental and theoretical efforts. 12,21

To demonstrate that theory can help us understand the electrostatic environment within a coacervate, we show that our transfer matrix method yields phase behavior consistent with the experimental data in Figures 4a,b. As described in the Methods section, we use a Monte Carlo algorithm and the free energy in eq 5 to find the coexisting coacervate and supernatant phase compositions. We run these calculations starting at a low polymer concentration $\phi_{\rm p}$ = 0.01 and then systematically increase the salt concentration $\phi_{\rm S}$. A system undergoing phase separation will equilibrate to two phases α and β with significantly different values of $\phi_{\rm p}^{\alpha} \neq \phi_{\rm p}^{\beta}$; however, with increasing salt concentration, these values become increasingly close. We approximately relate this to turbidity by quantifying the difference in the water concentrations between the two phases $\phi_{\rm W}^{\alpha} - \phi_{\rm W}^{\beta} = \Delta \phi_{\rm W}$, as the concentration of water will be the primary factor in the refractive index differences between the phases that are responsible for turbid coacervates. We choose to use a value $\alpha = 100\% \times (1 - e^{-\mathcal{A}\Delta\phi_{W}^{2}})$ that maps the compositional difference to the scale of the optical measurement using an empirical parameter $\mathcal{A} = 5000$. This is a nonrigorous

mapping, 76,77 but it is motivated by the relationships between dielectric constant mismatch and turbidity in the light scattering literature and reaches the appropriate limits of $\Delta\phi_{
m W}$ o 0 and $\Delta\phi_{
m W}$ o ∞ as 0% and 100% turbidity, respectively. The results are plotted in Figures 4c and 4d for the K10 and K30 series, respectively, showing that our model can indeed exhibit phase behavior consistent with the experiments in Figures 4a and 4b. Similar to the experimental data, an increase in the length of either the polyK or the polyD leads to an increase in the salt resistivity. It is not prudent to make a quantitative comparison between these plots, however, due to (1) the empirical mapping between turbidity and $\Delta\phi_{\rm W}$ and (2) the need to parametrize the relationship between the molar concentration of salt and polymer in the experiment versus the volume fractions of the same species in theory. Nevertheless, these results establish a qualitative consistency between the experimental peptide-based coacervate system and the transfer matrix model.

The qualitative agreement between salt stability behaviors observed in experiment and theory, shown in Figure 4, allows us to predict full coacervation phase diagrams as a function of length mismatch in polypeptide pairs (Figure 5). It is experimentally impractical to obtain these phase diagrams due to the technical challenges involved with measuring the polymer and salt concentrations in both the coacervate and dilute phases for small sample volumes. However, the thermodynamic predictions from our theoretical model allow us to determine the conditions in the polymer-rich coacervate and polymer-dilute supernatant relevant to our experimental measurements of their local electrostatic environments. We plot phase diagrams in Figures 5a and 5b for K10 and K30, respectively, as calculated using the transfer matrix model. For both polycation lengths, we see that the two-phase coexistence region expands with a concomitant increase in polyanion length. We break down each term in eq 5 in the Supporting Information (Figure S6) to illustrate the principal contributions to phase separation and to show that the polyanion and polycation lengths affect phase separation via their mixing entropy terms. We indicate in Figure 5 the conditions where we performed the salt stability calculations in Figure 4 and

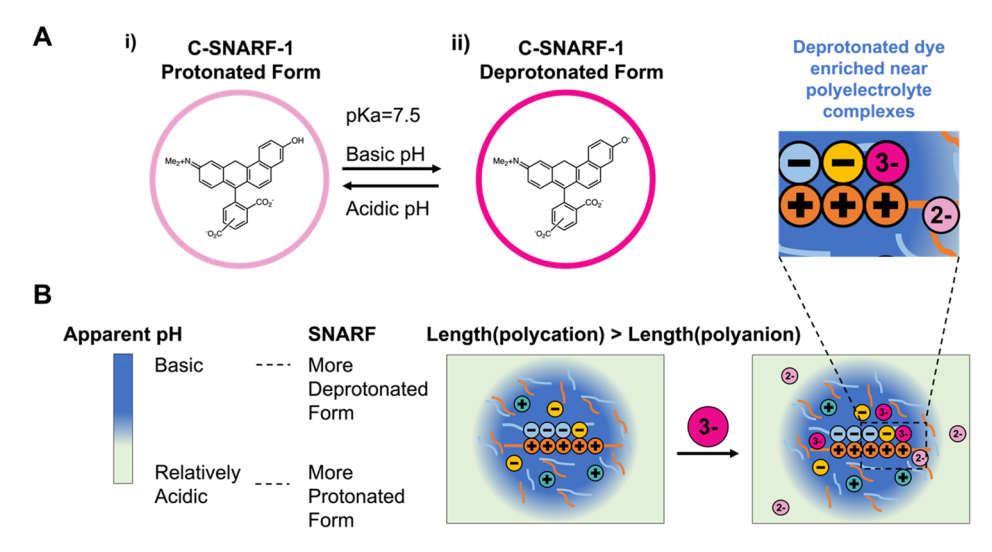


Figure 6. Relationship between the apparent pH and molecular-level (de)protonation equilibrium. (A) Chemical structure of SNARF in the protonated and deprotonated states, with the dilute solution $pK_a = 7.5$ between the two states leading to two different fluorescence spectra (similar to the colored circle representation). (B) Schematic illustration of SNARF's local distribution in the coacervate phase versus dilute phase, as depicted by the color gradients in the calibration bar. The key difference between the two phases, which report different effective pH values, is that the high charge density of polycations in the coacervate phase stabilizes the deprotonated form.

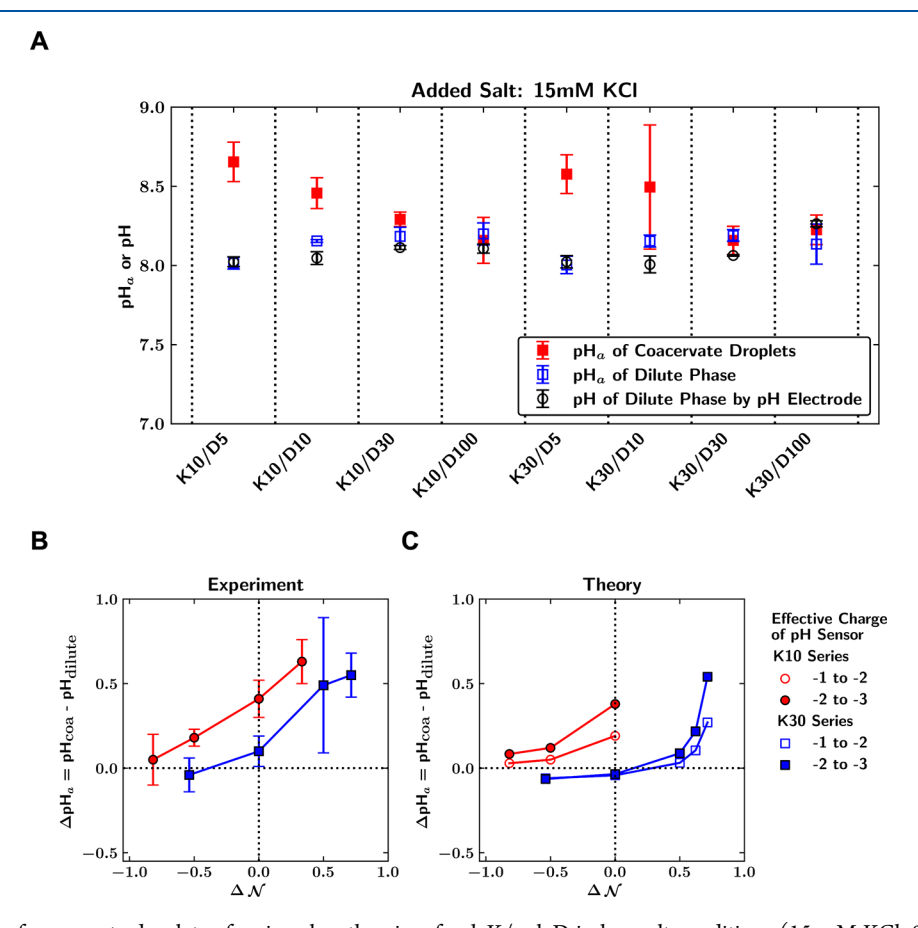


Figure 7. Apparent pH of coacervate droplets of various length pairs of polyK/polyD in low salt conditions (15 mM KCl, 0.5 mM MgCl₂, 10 mM Tris buffer). (A) Local apparent pH of coacervate droplets of K10 and K30 in low salt. Adapted with permission from ref 12. Copyright 2020 Springer Nature. K10/D30, K10/D100, K30/D10, and K30/D100 are newly included here. Plot of local apparent pH difference between coacervate phase and dilute phase (Δ pH_{eff}) as a function of length asymmetry by the (B) experiment and (C) theory. Experimental apparent pH values of K10/D5, K10/D10, and K30/D30 are replotted using values in our previous study. Experimental values are calculated using 45 ROIs each for the coacervate droplets and dilute phase from three images of three independent samples. Error bars of experimental values indicate the standard deviation of values.

note that the dramatic decrease in α corresponds to the binodal curve that demarcates the phase coexistence; this again moves to higher salt concentration with increasing polyanion and polycation length. Notably, the critical salt concentration of coacervation appears to be more sensitive to the length of the shorter polyelectrolyte. For example, the coexistence region for K10/D100 in Figure 5a is significantly smaller than the coexistence region for K30/D30 in Figure 5b, with the increase in the polyK length from 10 to 30 being more important for the phase behavior than the decrease in the polyD length from 100 to 30. These trends are broadly expected based on the increasing importance of the translational entropy at small chain lengths, which has been seen in the experimental and theoretical literature as phase diagrams exhibiting chain-lengthdependent effects for small chains <50 monomeric units long. 20,21,38 Also consistent with prior literature is the prediction that the tie lines connecting two coexisting states exhibit negative slopes, indicating preferential salt partitioning into the supernatant phase. While we do not quantify salt partitioning in this study, the negative slope of the tie lines is consistent with experimental phase diagrams of coacervation including those formed by polypeptides (i.e., polyK and polyglutamic acids).^{21,38}

Despite several points of qualitative agreement between the experiment and theory, we do note that this thermodynamic model does not account for specific chemical group effects. Our model would predict the same phase diagrams for symmetric polyelectrolyte pairs K10/D30 and K30/D10; however, we note that the experimental salt stability behaviors of K10/D30 and K30/D10 are different (Figure 4a,b and Table S1). We attribute this disparity to chemical differences not considered in our theoretical model, such as differences in charge solvation or specific ion effects, which would require more detailed molecular simulation or extensive parametrization to account for this non-negligible experimental observation. Nevertheless, by integrating our theoretical model with fluorescence measurements, we do not need this level of chemical detail to obtain insights into how different length pairs of polyK and polyD affect the local electrostatic environment within the coacervate phase.

Local Apparent pH of Coacervates by Length-Mismatched Polyelectrolyte Pairs. To investigate the coacervate microenvironment as a function of polyK and polyD length, we used 5-(and 6)-carboxy SNARF-1 (SNARF), which is a widely used ratiometric pH indicator that is less sensitive to different levels of partitioning to measure local pH in cells⁷⁸ or polymer microspheres⁷⁹ and on charged surface nanoparticles. 80 The local apparent pH of both the coacervate phase and dilute phases can be estimated by the ratio of the fluorescence intensity of dual emission peaks corresponding to protonated and deprotonated statues of SNARF (see more details in the Methods section, Figure 6a). The equilibrium between these states is sensitive to the local electrostatic environment; for example, if SNARF localized near an oppositely charged polyelectrolyte within a coacervate is more deprotonated than in dilute solution, the local apparent pH of that microenvironment will be reported as more basic (Figure 6b). We previously observed that for coacervates composed of polyK and polyD, SNARF indeed reports a more basic environment than the coexisting supernatant phase. This is ostensibly due to differences in the local electrostatic environment, in particular when SNARF is localized near the oppositely charged polyelectrolyte as indicated in Figure 6b.

ı

We consider the hypothesis that strong electrostatic interactions of the dye with charged monomers affect the protonation equilibrium of SNARF that is interpreted as a change in the apparent pH.

We use the molecular weights (lengths) of the coacervateforming polyelectrolyte species as a parameter to vary the physical state of the coacervate and thus indirectly probe the local electrostatics responsible for the apparent pH change. Previous work by some of the authors has demonstrated, in certain cases, that a significant physical change can be induced that leads to large apparent pH shifts. In Figure 7a, we plot the apparent pH shifts for several combinations of polyK and polyD lengths; as a reference, we directly measure the pH of the dilute phase (open circles) and compare them with the ratiometric pH from SNARF (blue, open squares). There is agreement between these two measurements, confirming the ability of SNARF to accurately measure the apparent pH. We also plot the apparent pH of the polymer-dense coacervate droplets (red, filled squares), which for several situations exhibit significant deviations from the apparent pH of the dilute phase. The extent of these deviations depends on the specific combination of chain lengths of the polypeptides, and so we plot in Figure 7b the difference between the dilute and coacervate phase apparent pH values $(\Delta pH_a = pH_c - pH_s)$ versus a metric describing the chain length disparity $\Delta N = (N_{P+} - N_{P-})/(N_{P+} + N_{P-})$ and generally increases (decreases) with the length of the polyK (polyD). For both the K10 and K30 series, we observe a monotonic increase in ΔpH_a with ΔN , which for a given polyK is associated with a decrease in the chain length of the polyD. This means that deviations from the dilute solution pH are exacerbated when the length of the polyD becomes small. Similarly, the K10 series exhibits a larger ΔpH_a than that of the K30 series, such that this is true for the polyK as well.

We use our theoretical transfer matrix model, described in detail in the Methods section, to suggest a mechanism for this behavior consistent with the experimental data. The ΔpH_a represents how the equilibrium between the two protonation states is affected by the surrounding electrostatic environment. Taking the pH_s as a reference for the protonation equilibrium in dilute solution, we assume that the highly charged, deprotonated state of SNARF is stabilized when it is adjacent to a polyelectrolyte of the opposite charge. In the Methods section, we describe how we quantify the equilibrium between a "free" SNARF molecule far away from the polyelectrolyte and a "paired" SNARF molecule that is localized near these same chains. In the coacervate phase, the finite concentration of the polycation leads to an abundance of available pairing locations for SNARF, which appears more basic due to the consequent stabilization of the deprotonated state. In Figure 7c, we plot the results of these calculations for mismatched chain lengths on the same ΔpH_a versus ΔN plot considered in Figure 7b. This is done for two situations: one in which the SNARF molecule can be in either -2 or -3 charge states (filled symbols) and one in which it can be in either -1 or -2 charge states (open symbols). These situations represent different options for how SNARF interacts with the polycation; the -1/-2 version assumes that the polycation interacts with the overall charge on the dye molecule, while the -2/-3 version assumes that the polycation interacts with the side of the molecule with negatively charged moieties and the positively charged (imine) group does not participate. The magnitude of the ΔpH_a shift in the experiment appears to be more

consistent with the second option, though both situations show similar trends.

Our theoretical argument suggests that there are two features affecting the $\Delta p H_a$ shift: (1) the fraction of paired versus open sites on the polycation and (2) the concentration of the polycation itself. These are accounted for in the parenthetical factor and ϕ_{P+} factor, respectively, in eq 7, and we argue that through both of these mechanisms the apparent pH shift is almost entirely attributable to the concentration of the coacervate phase. This is shown to be plausible in the experiment, which shows a shift in the dye pK_a in the presence of pure polycation (K10, Figure S7). To demonstrate this relationship, we plot $\Delta p H_a$ versus ϕ_{P+} in Figure 8 for the

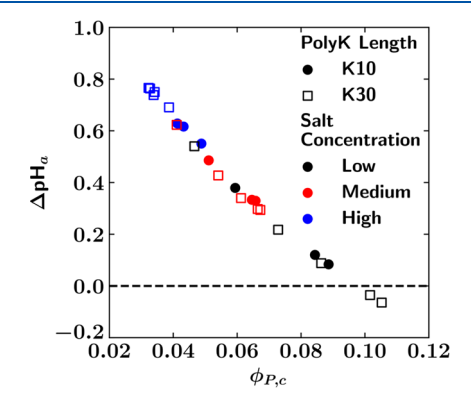
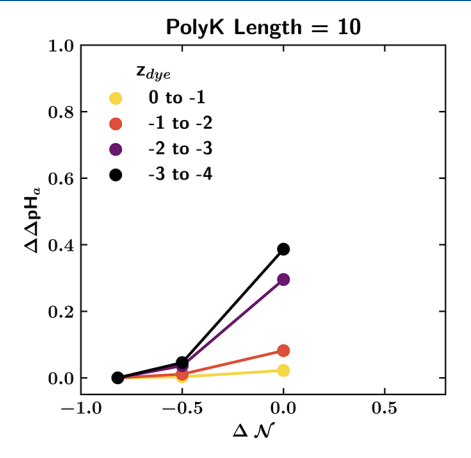


Figure 8. Theoretical prediction for the apparent ΔpH_a of coacervate droplets versus the coacervate polycation density ϕ_{P+} for several lengths of polyK and polyD as well as salt concentrations. We plot both different lengths of polyK and polyD (distinguishing K10, filled circles, and K30, open squares) and salt concentrations (with different colors corresponding to low, medium, and high salt concentrations). A detailed accounting and discussion of the specific length and salt conditions is included in the Supporting Information (Table S2). All of these conditions exhibit a collapse to a single curve, demonstrating that polycation density ϕ_{P+} is the primary determinant of the apparent pH shift and leading us to attribute this shift to the local concentrations of polycation sites that can stabilize the negatively charged dye in its deprotonated state.

theoretical predictions for several combinations of chain length and salt concentration. We briefly note that we did not consider salt concentration in the experiments but can straightforwardly include in our theory to show that ΔpH_a increases with salt concentration and supports the generality of our conclusions. Indeed, all these systems exhibit a near collapse onto a single curve. Some subtle differences are apparent, with K10 points being slightly higher than K30 points, but the collapse is excellent over essentially the entire parameter space we consider. We note that this connects something we can measure experimentally (the ΔpH_a shift) to something that is difficult to measure directly (the concentration ϕ_{P^+} in the coacervate phase) and that an increase in the former corresponds to a decrease in the latter. The consequences of this are 2-fold: First, any probe-based measure of local pH may not be measured by pH but rather the specifics of its interaction with the dense, polyelectrolyte-rich milieu of the coacervate phase. Indeed, we contend that the apparent shift in pH (ΔpH_a) is better thought of as a shift in the p K_a of SNARF, as our model did not require that the actual pH (i.e., the concentration of H+ ions) is changing. Second, while a quantitative connection would require parametrization and/or calibration, pH probes may be a useful way to report on phase composition through this pK_a shift in situations where the polymer concentration is otherwise inaccessible.

Effect of Dye Size and Charge on ΔpH_a Shift. We demonstrated that in a dense coacervate phase the protonation-deprotonation equilibrium of the pH-sensitive dye SNARF can be affected by strong electrostatic interactions with the oppositely charged polyelectrolyte species. This serves as a proxy for coacervate concentration, but we also expect this effect to be generalizable to other dyes and sensitive to the strength of the electrostatic attractions between the polyelectrolyte and dye species. While this is challenging to systematically adjust in an experiment, without the complicating effects of solvation due to changes in chemistry, we can consider how changes in the dye affect theoretical predictions. Dye electrostatic effects enter in two places in our formalism. First, the attractive Coulomb energy given in eq 9 is a function of both the valency of the charge z_{Dye} and the interaction distance between the two species $\sigma_{\rm int}$. Second, there is a



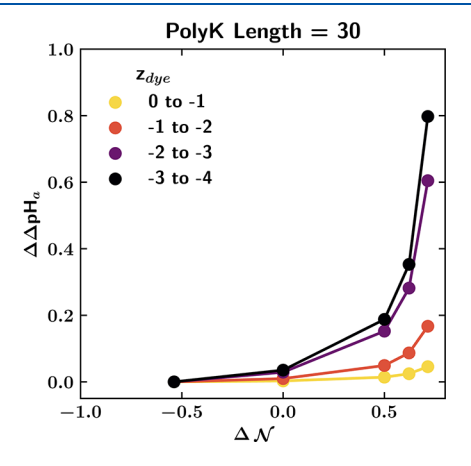
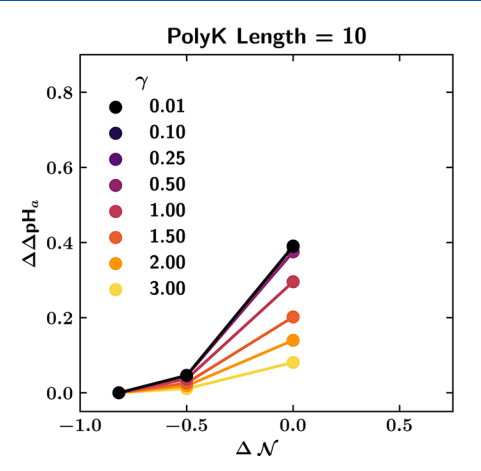


Figure 9. Theoretical prediction of the shift in apparent pH for guest molecules of different charge valencies. The apparent shift in pH $\Delta\Delta$ pH_a is normalized to a reference at the smallest value of $\Delta\mathcal{N}$ and is plotted for the K10 (A) and K30 (B) series. Purple symbols are the apparent pH difference values shown in Figure 7, using the charge valencies -2 to -3. In general, an increase in the valency corresponds to larger shifts in the apparent pH, which we attribute to the larger electrostatic stabilization of the guest molecule by the oppositely charged polyelectrolyte in the coacervate.



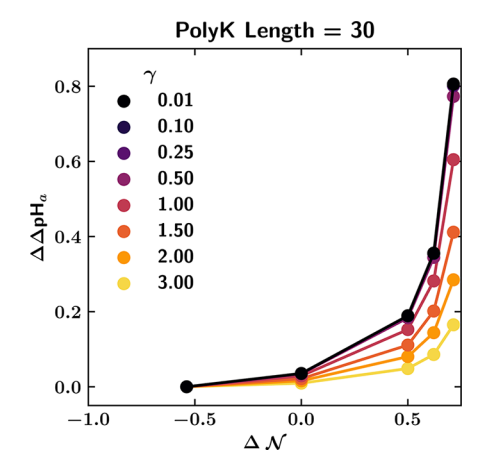


Figure 10. Theoretical prediction for the shift in apparent pH for guest molecules of different relative molecular size γ . The apparent shift in pH $\Delta\Delta pH_a$ is normalized to a reference at the smallest value of ΔN and is plotted for the K10 (A) and K30 (B) series. Black symbols are the apparent pH difference values shown in Figure 7, with the size chosen by SNARF-1 that serves as the reference (so $\gamma = 1$). In general, a decrease in the valency corresponds to larger shifts in the apparent pH due to the stronger electrostatic interactions with the guest molecule and the oppositely charged polyelectrolyte in the coacervate.

valency-dependent prefactor in eq 10 that accounts for the simultaneous binding of the dye to multiple connected polyelectrolyte monomers, which using typical ion pairing arguments effectively increases the valency of the polymer to match the valency of the SNARF molecule.

We have been focusing on the specific valency of the pHsensitive dye SNARF ($z_{\rm dye} = -2$ versus $z_{\rm dye} = -3$), but other pH-sensitive dyes could be selected that are in equilibrium between states of different valencies. We can include this more general case by modifying eqs 9 and 10, through both the value of $q_{\rm Dye}$ and the prefactor in the Boltzmann factor in eq 10. Because we assume that a small amount of dye does not affect the equilibrium phase behavior of coacervates, we can immediately calculate the ΔpH_a as a function of $\Delta \mathcal{N}$ for several different sets of valencies for both the K10 and K30 series (in Figures 9a and 9b, respectively). We normalize these trends to facilitate comparison between the different situations by normalizing to the leftmost point $(\Delta pH_{a,ref})$ in each series to obtain $\Delta \Delta pH_a = \Delta pH_a - \Delta pH_{a,ref}$. We justify this comparison by noting that the vertical shift of the overall curve of ΔpH_a versus ΔN is set primarily by a phenomenological energy parameter βE_{ϵ} that accounts for solubility differences that are dye-specific. We observe that for increasing valency both series exhibit a much more pronounced shift $\Delta\Delta pH_a$ that we attribute to the increased stabilization of the more highly charged polycation-bound state. Interestingly, in the limit in which the change in valency goes between $z_{dve} = 0$ and $z_{\text{dye}} = -1$, there is very little shift in the apparent pH. This provides the straightforward prediction that the sensitivity of a dye such as SNARF to the electrostatic environment will depend on its net charge.

This effect is also apparent when the size of the charge $r_{\rm Dye}$ is changed. This similarly changes the electrostatic ion pairing energy in eq 9, but this time through modification of the interaction distance in the denominator. In Figures 9a and 9b we show how the $\Delta\Delta$ pH_a versus ΔN plots are affected by the relative size $\gamma = \sigma_{\rm Dye} / \sigma_{\rm Dye,0}$, where $\sigma_{\rm Dye,0}$ is the reference size used for SNARF. For both K10 (Figure 9a) and K30 (Figure 9b), there is a monotonic increase in the pH shift with a decreasing relative size. This is fully consistent with our predictions for valency, as a decrease in size increases the pairing energy at contact between the two charged species. In

contrast, large dyes ($\gamma = 3$) show significantly less pH shift, as the chain—dye contact energy is weak in this case.

CONCLUSION

We used a combination of experiment and theory to understand how the local electrostatic environment within polyelectrolyte coacervates can govern the behavior of pHsensitive dye molecules. By tuning the length of oppositely charged polypeptide chains, polyK and polyD, we can change the density of the coacervate phase and show that there is an apparent shift in the ratiometric pH indicator SNARF. We see a correlation between the strength of phase separation, as determined from turbidity measurements, and the apparent pH shift. To understand this phenomenon, we establish qualitative agreement between experimental salt resistance and the transfer matrix theory of coacervation. This allows us to predict the composition and thermodynamics of the dense coacervate phase, which we then use to develop a three-state model of protonation-deprotonation equilibria in a pHsensitive dye such as SNARF-1. In addition to protonated and deprotonated states, we consider a state where the charged dye is "paired" with and then stabilized by the oppositely charged polyelectrolyte. This biases the SNARF molecule toward the more highly charged state. This simple model can reproduce the behaviors observed in the experiment, with qualitative agreement between the apparent pH shift and the length mismatch of the polypeptide chains.

Using experiment and theory, we demonstrate that pH-sensitive dyes such as SNARF can register significant shifts in pH in a coacervate phase, but this represents a shift in the pK_a induced by the local electrostatic environment. Instead, the fluorescence of SNARF is determined almost completely by the concentration of oppositely charged polypeptides that can electrostatically stabilize the highly charged state. We also predict that the extent of this effect can be significantly affected by the features of the dye, such as the valency and size, which determine the strength of the polyelectrolyte—dye Coulomb attractions. Such an understanding can inform efforts to minimize this effect, for example, by considering less-charged molecules as indicators of the local microenvironment. It can also point to scenarios where larger impacts can be anticipated; for example, guest molecules having higher total charge and

charge densities particularly for complex coacervates having high densities of oppositely charged polyions are more likely to experience changes in their charge equilibria.

By comparing the apparent pH values reported by guest molecules between coacervate and dilute phases, we can begin to understand the local electrostatics of molecules sequestered in the coacervate phase. Similar cases can be found in the literature where pH-sensitive dyes were used to sense local interactions between protein-ligand on supported lipid bilayers or between small molecules and lipid layers.^{81,82} Agreement between experimental observations and theoretical calculations suggests that this effect is general when small molecules accumulate in dense coacervate phases. Small molecules would experience different local electrostatic environments as they actively interact with polyelectrolytes in coacervates, which may affect their state or function. In this case, the protonation state was perturbed, but in general guest molecules such as metabolites, 83 drugs, 84 or metal ions 85 may have other functional properties affected by local electrostatics within phase separating compartments. This would also have important ramifications for systems, such as biomolecular condensates, where biological function may be sensitive to electrostatics in phase-separating regions analogous to the coacervates considered in this paper.

ASSOCIATED CONTENT

Supporting Information

The Supporting Information is available free of charge at https://pubs.acs.org/doi/10.1021/acs.jpcb.3c02098.

Table and graphs showing calibration of local apparent pH measurements in coacervates, controlled experiments, term-by-term breakdown of the second derivative of the free energy terms, and critical salt concentrations for coacervation from fitting parameters of experimental curves and theoretical predicted values (PDF)

AUTHOR INFORMATION

Corresponding Authors

Charles E. Sing — Department of Chemical and Biomolecular Engineering and Beckman Institute for Advanced Science and Technology, University of Illinois at Urbana—Champaign, Urbana, Illinois 61801, United States; orcid.org/0000-0001-7231-2685; Email: cesing@illinois.edu

Christine D. Keating — Department of Chemistry, The Pennsylvania State University, University Park, Pennsylvania 16802, United States; orcid.org/0000-0001-6039-1961; Email: keating@chem.psu.edu

Authors

Saehyun Choi – Department of Chemistry, The Pennsylvania State University, University Park, Pennsylvania 16802, United States; Present Address: Department of Chemistry, University of California, Berkeley, Berkeley, CA 94720

Ashley R. Knoerdel – Program in Biophysics and Quantitative Biology, University of Illinois at Urbana–Champaign, Urbana, Illinois 61801, United States

Complete contact information is available at: https://pubs.acs.org/10.1021/acs.jpcb.3c02098

Author Contributions

These authors contributed equally.

Notes

The authors declare no competing financial interest.

■ ACKNOWLEDGMENTS

A.R.K. and C.E.S. acknowledge support from the National Science Foundation under grant DMR-1654158. S.C. and C.D.K. acknowledge support from the NASA Exobiology program grant no. 80NSSC17K0034 and no. 80NSSC22K0553. S.C. was also supported by Future Investigators in NASA Earth and Space Science and Technology (FINESST) under no. 80NSSC19K1531.

REFERENCES

- (1) de Jong, H. G. B.; Kruyt, H. R. Coacervation (partial miscibility on colloid systems) (preliminary communication). *Proceedings of the Koninklijke Akademie Van Wetenschappen Te Amsterdam* **1929**, 32 (6/10), 849–856.
- (2) Yewdall, N. A.; André, A. A. M.; Lu, T.; Spruijt, E. Coacervates as models of membraneless organelles. *Curr. Opin. Colloid Interface Sci.* **2021**, *52*, 101416.
- (3) Poudyal, R. R.; Pir Cakmak, F.; Keating, C. D.; Bevilacqua, P. C. Physical Principles and Extant Biology Reveal Roles for RNA-Containing Membraneless Compartments in Origins of Life Chemistry. *Biochemistry* **2018**, *57* (17), 2509–2519.
- (4) Sing, C. E.; Perry, S. L. Recent progress in the science of complex coacervation. *Soft Matter* **2020**, *16* (12), 2885–2914.
- (5) Tang, T.-Y. D.; Antognozzi, M.; Vicary, J. A.; Perriman, A. W.; Mann, S. Small-molecule uptake in membrane-free peptide/nucleotide protocells. *Soft Matter* **2013**, *9* (31), 7647–7656.
- (6) Dora Tang, T. Y.; Rohaida Che Hak, C.; Thompson, A. J.; Kuimova, M. K.; Williams, D. S.; Perriman, A. W.; Mann, S. Fatty acid membrane assembly on coacervate microdroplets as a step towards a hybrid protocell model. *Nat. Chem.* **2014**, *6* (6), 527–33.
- (7) Smokers, I. B. A.; van Haren, M. H. I.; Lu, T.; Spruijt, E. Complex Coacervation and Compartmentalized Conversion of Prebiotically Relevant Metabolites. *ChemSystemsChem* **2022**, *4* (4), No. e202200004.
- (8) Love, C.; Steinkühler, J.; Gonzales, D. T.; Yandrapalli, N.; Robinson, T.; Dimova, R.; Tang, T. Y. D. Reversible pH-Responsive Coacervate Formation in Lipid Vesicles Activates Dormant Enzymatic Reactions. *Angew. Chem.* **2020**, *132* (15), 6006–6013.
- (9) Roberts, S.; Dzuricky, M.; Chilkoti, A. Elastin-like polypeptides as models of intrinsically disordered proteins. *FEBS Lett.* **2015**, *589*, 2477–2486.
- (10) Drobot, B.; Iglesias-Artola, J. M.; Le Vay, K.; Mayr, V.; Kar, M.; Kreysing, M.; Mutschler, H.; Tang, T. D. Compartmentalised RNA catalysis in membrane-free coacervate protocells. *Nat. Commun.* **2018**, 9 (3643), 3643.
- (11) Iglesias-Artola, J. M.; Drobot, B.; Kar, M.; Fritsch, A. W.; Mutschler, H.; Dora Tang, T. Y.; Kreysing, M. Charge-density reduction promotes ribozyme activity in RNA-peptide coacervates via RNA fluidization and magnesium partitioning. *Nat. Chem.* **2022**, *14* (4), 407–416.
- (12) Cakmak, F. P.; Choi, S.; Meyer, M. O.; Bevilacqua, P. C.; Keating, C. D. Prebiotically-relevant low polyion multivalency can improve functionality of membraneless compartments. *Nat. Commun.* **2020**, *11* (1), 5949.
- (13) Choi, S.; Meyer, M. O.; Bevilacqua, P. C.; Keating, C. D. Phase-specific RNA accumulation and duplex thermodynamics in multiphase coacervate models for membraneless organelles. *Nat. Chem.* **2022**, *14* (10), 1110–1117.
- (14) Fares, H. M.; Marras, A. E.; Ting, J. M.; Tirrell, M. V.; Keating, C. D. Impact of wet-dry cycling on the phase behavior and compartmentalization properties of complex coacervates. *Nat. Commun.* **2020**, *11* (1), 5423.
- (15) Black, K. A.; Priftis, D.; Perry, S. L.; Yip, J.; Byun, W. Y.; Tirrell, M. Protein Encapsulation via Polypeptide Complex Coacervation. *ACS Macro Lett.* **2014**, 3 (10), 1088–1091.

- (16) Nakashima, K. K.; Baaij, J. F.; Spruijt, E. Reversible generation of coacervate droplets in an enzymatic network. *Soft Matter* **2018**, *14* (3), 361–367.
- (17) Martin, N.; Li, M.; Mann, S. Selective uptake and refolding of globular proteins in coacervate microdroplets. *Langmuir* **2016**, 32 (23), 5881–5889.
- (18) Poudyal, R. R.; Guth-Metzler, R. M.; Veenis, A. J.; Frankel, E. A.; Keating, C. D.; Bevilacqua, P. C. Template-directed RNA polymerization and enhanced ribozyme catalysis inside membraneless compartments formed by coacervates. *Nat. Commun.* **2019**, *10*, 490.
- (19) Poudyal, R. R.; Keating, C. D.; Bevilacqua, P. C. Polyanion-assisted ribozyme catalysis inside complex coacervates. *ACS Chem. Biol.* **2019**, *14* (6), 1243–1248.
- (20) Spruijt, E.; Westphal, A. H.; Borst, J. W.; Cohen Stuart, M. A.; van der Gucht, J. Binodal Compositions of Polyelectrolyte Complexes. *Macromolecules* **2010**, *43* (15), 6476–6484.
- (21) Li, L.; Srivastava, S.; Andreev, M.; Marciel, A. B.; de Pablo, J. J.; Tirrell, M. V. Phase Behavior and Salt Partitioning in Polyelectrolyte Complex Coacervates. *Macromolecules* **2018**, *51* (8), 2988–2995.
- (22) Spruijt, E.; Cohen Stuart, M. A.; van der Gucht, J. Linear Viscoelasticity of Polyelectrolyte Complex Coacervates. *Macromolecules* **2013**, *46* (4), 1633–1641.
- (23) Liu, Y.; Santa Chalarca, C. F.; Carmean, R. N.; Olson, R. A.; Madinya, J.; Sumerlin, B. S.; Sing, C. E.; Emrick, T.; Perry, S. L. Effect of Polymer Chemistry on the Linear Viscoelasticity of Complex Coacervates. *Macromolecules* **2020**, 53 (18), 7851–7864.
- (24) Han, J.; Burgess, K. Fluorescent Indicators for Intracellular pH. Chem. Rev. 2010, 110 (5), 2709–2728.
- (25) Murmiliuk, A.; Košovan, P.; Janata, M.; Procházka, K.; Uhlík, F.; Štěpánek, M. Local pH and Effective pK of a Polyelectrolyte Chain: Two Names for One Quantity? *ACS Macro Lett.* **2018**, *7* (10), 1243–1247.
- (26) Hartley, G. S.; Roe, J. W. Ionic concentrations at interfaces. *Trans. Faraday Soc.* **1940**, 35 (0), 101–109.
- (27) Zhang, Y.; Wang, Q.; Hess, H. Increasing Enzyme Cascade Throughput by pH-Engineering the Microenvironment of Individual Enzymes. ACS Catal. 2017, 7 (3), 2047–2051.
- (28) Ma, X.; Wang, Y.; Zhao, T.; Li, Y.; Su, L.-C.; Wang, Z.; Huang, G.; Sumer, B. D.; Gao, J. Ultra-pH-Sensitive Nanoprobe Library with Broad pH Tunability and Fluorescence Emissions. *J. Am. Chem. Soc.* **2014**, *136* (31), 11085–11092.
- (29) Anees, P.; Zhao, Y.; Greschner, A. A.; Congdon, T. R.; de Haan, H. W.; Cottenye, N.; Gauthier, M. A. Evidence, Manipulation, and Termination of pH 'Nanobuffering' for Quantitative Homogenous Scavenging of Monoclonal Antibodies. *ACS Nano* **2019**, *13* (2), 1019–1028.
- (30) Tao, W.; Wang, J.; Parak, W. J.; Farokhzad, O. C.; Shi, J. Nanobuffering of pH-Responsive Polymers: A Known but Sometimes Overlooked Phenomenon and Its Biological Applications. *ACS Nano* **2019**, *13* (5), 4876–4882.
- (31) Digby, Z. A.; Yang, M.; Lteif, S.; Schlenoff, J. B. Salt Resistance as a Measure of the Strength of Polyelectrolyte Complexation. *Macromolecules* **2022**, *55* (3), 978–988.
- (32) Choi, J.; Rubner, M. F. Influence of the Degree of Ionization on Weak Polyelectrolyte Multilayer Assembly. *Macromolecules* **2005**, 38 (1), 116–124.
- (33) Alonso, T.; Irigoyen, J.; Iturri, J. J.; larena, I. L.; Moya, S. E. Study of the multilayer assembly and complex formation of poly(diallyldimethylammonium chloride) (PDADMAC) and poly-(acrylic acid) (PAA) as a function of pH. *Soft Matter* **2013**, 9 (6), 1920–1928.
- (34) Knoerdel, A. R.; Blocher McTigue, W. C.; Sing, C. E. Transfer Matrix Model of pH Effects in Polymeric Complex Coacervation. *J. Phys. Chem. B* **2021**, *125* (31), 8965–8980.
- (35) Isom, D. G.; Castañeda, C. A.; Cannon, B. R.; García-Moreno E, B. Large shifts in pKa values of lysine residues buried inside a protein. *Proc. Natl. Acad. Sci. U. S. A.* **2011**, *108* (13), 5260.

- (36) Kuhn, B.; Kollman, P. A.; Stahl, M. Prediction of pKa shifts in proteins using a combination of molecular mechanical and continuum solvent calculations. *J. Comput. Chem.* **2004**, *25* (15), 1865–1872.
- (37) Longo, G. S.; Olvera de la Cruz, M.; Szleifer, I. Molecular Theory of Weak Polyelectrolyte Gels: The Role of pH and Salt Concentration. *Macromolecules* **2011**, 44 (1), 147–158.
- (38) Radhakrishna, M.; Basu, K.; Liu, Y.; Shamsi, R.; Perry, S. L.; Sing, C. E. Molecular Connectivity and Correlation Effects on Polymer Coacervation. *Macromolecules* **2017**, *50* (7), 3030–3037.
- (39) Andreev, M.; Prabhu, V. M.; Douglas, J. F.; Tirrell, M.; de Pablo, J. J. Complex Coacervation in Polyelectrolytes from a Coarse-Grained Model. *Macromolecules* **2018**, *51* (17), 6717–6723.
- (40) Lytle, T. K.; Salazar, A. J.; Sing, C. E. Interfacial properties of polymeric complex coacervates from simulation and theory. *J. Chem. Phys.* **2018**, *149* (16), 163315.
- (41) Lytle, T. K.; Chang, L.-W.; Markiewicz, N.; Perry, S. L.; Sing, C. E. Designing Electrostatic Interactions via Polyelectrolyte Monomer Sequence. ACS Cent. Sci. 2019, 5 (4), 709–718.
- (42) Mintis, D. G.; Mavrantzas, V. G. Phase Boundary and Salt Partitioning in Coacervate Complexes Formed between Poly(acrylic acid) and Poly(N,N-dimethylaminoethyl methacrylate) from Detailed Atomistic Simulations Combined with Free Energy Perturbation and Thermodynamic Integration Calculations. *Macromolecules* **2020**, *53* (18), 7618–7634.
- (43) Hoffmann, K. Q.; Perry, S. L.; Leon, L.; Priftis, D.; Tirrell, M.; de Pablo, J. J. A molecular view of the role of chirality in charge-driven polypeptide complexation. *Soft Matter* **2015**, *11* (8), 1525–1538.
- (44) Borue, V. Y.; Erukhimovich, I. Y. A statistical theory of globular polyelectrolyte complexes. *Macromolecules* **1990**, 23 (15), 3625–3632
- (45) Castelnovo, M.; Joanny, J. F. Complexation between oppositely charged polyelectrolytes: Beyond the Random Phase Approximation. *Eur. Phys. J. E* **2001**, *6* (1), 377–386.
- (46) Kudlay, A.; Olvera de la Cruz, M. Precipitation of oppositely charged polyelectrolytes in salt solutions. *J. Chem. Phys.* **2004**, *120* (1), 404–412.
- (47) Qin, J.; de Pablo, J. J. Criticality and Connectivity in Macromolecular Charge Complexation. *Macromolecules* **2016**, 49 (22), 8789–8800.
- (48) Lee, J.; Popov, Y. O.; Fredrickson, G. H. Complex coacervation: A field theoretic simulation study of polyelectrolyte complexation. *J. Chem. Phys.* **2008**, *128* (22), 224908.
- (49) Riggleman, R. A.; Kumar, R.; Fredrickson, G. H. Investigation of the interfacial tension of complex coacervates using field-theoretic simulations. *J. Chem. Phys.* **2012**, *136* (2), 024903.
- (50) Danielsen, S. P. O.; McCarty, J.; Shea, J.-E.; Delaney, K. T.; Fredrickson, G. H. Small ion effects on self-coacervation phenomena in block polyampholytes. *J. Chem. Phys.* **2019**, *151* (3), 034904.
- (51) Shusharina, N. P.; Zhulina, E. B.; Dobrynin, A. V.; Rubinstein, M. Scaling Theory of Diblock Polyampholyte Solutions. *Macromolecules* **2005**, 38 (21), 8870–8881.
- (52) Wang, Z.; Rubinstein, M. Regimes of Conformational Transitions of a Diblock Polyampholyte. *Macromolecules* **2006**, 39 (17), 5897–5912.
- (53) Rubinstein, M.; Liao, Q.; Panyukov, S. Structure of Liquid Coacervates Formed by Oppositely Charged Polyelectrolytes. *Macromolecules* **2018**, *51* (23), 9572–9588.
- (54) Neitzel, A. E.; Fang, Y. N.; Yu, B.; Rumyantsev, A. M.; de Pablo, J. J.; Tirrell, M. V. Polyelectrolyte Complex Coacervation across a Broad Range of Charge Densities. *Macromolecules* **2021**, *54* (14), 6878–6890.
- (55) Rumyantsev, A. M.; de Pablo, J. J. Liquid Crystalline and Isotropic Coacervates of Semiflexible Polyanions and Flexible Polycations. *Macromolecules* **2019**, 52 (14), 5140–5156.
- (56) Rumyantsev, A. M.; Kramarenko, E. Y.; Borisov, O. V. Microphase Separation in Complex Coacervate Due to Incompatibility between Polyanion and Polycation. *Macromolecules* **2018**, *51* (17), 6587–6601.

- (57) Zhang, P.; Alsaifi, N. M.; Wu, J.; Wang, Z.-G. Polyelectrolyte complex coacervation: Effects of concentration asymmetry. *J. Chem. Phys.* **2018**, *149* (16), 163303.
- (58) Perry, S. L.; Sing, C. E. PRISM-Based Theory of Complex Coacervation: Excluded Volume versus Chain Correlation. *Macromolecules* **2015**, *48* (14), 5040–5053.
- (59) Zhang, P.; Shen, K.; Alsaifi, N. M.; Wang, Z.-G. Salt Partitioning in Complex Coacervation of Symmetric Polyelectrolytes. *Macromolecules* **2018**, *51* (15), 5586–5593.
- (60) Friedowitz, S.; Lou, J.; Barker, K. P.; Will, K.; Xia, Y.; Qin, J. Looping-in complexation and ion partitioning in nonstoichiometric polyelectrolyte mixtures. *Sci. Adv.* **2021**, *7* (31), No. eabg8654.
- (61) Friedowitz, S.; Salehi, A.; Larson, R. G.; Qin, J. Role of electrostatic correlations in polyelectrolyte charge association. *J. Chem. Phys.* **2018**, 149 (16), 163335.
- (62) Lou, J.; Friedowitz, S.; Qin, J.; Xia, Y. Tunable Coacervation of Well-Defined Homologous Polyanions and Polycations by Local Polarity. ACS Cent. Sci. 2019, 5 (3), 549–557.
- (63) Friedowitz, S.; Qin, J. Reversible ion binding for polyelectrolytes with adaptive conformations. *AlChE J.* **2021**, 67 (12), No. e17426.
- (64) Salehi, A.; Larson, R. G. A Molecular Thermodynamic Model of Complexation in Mixtures of Oppositely Charged Polyelectrolytes with Explicit Account of Charge Association/Dissociation. *Macromolecules* **2016**, 49 (24), 9706–9719.
- (65) Ghasemi, M.; Friedowitz, S.; Larson, R. G. Analysis of Partitioning of Salt through Doping of Polyelectrolyte Complex Coacervates. *Macromolecules* **2020**, *53* (16), *6928*–*6945*.
- (66) Michaeli, I.; Overbeek, J. T. G.; Voorn, M. J. Phase separation of polyelectrolyte solutions. *J. Polym. Sci.* 1957, 23 (103), 443–450.
- (67) Overbeek, J. T. G.; Voorn, M. J. Phase separation in polyelectrolyte solutions. Theory of complex coacervation. *J. Cell. Compar. Physl.* **1957**, 49 (S1), 7–26.
- (68) Flory, P. J. Principles of Polymer Chemistry; Cornell University Press: Ithaca, NY, 1953.
- (69) Hückel, E.; Debye, P. The theory of electrolytes: I. lowering of freezing point and related phenomena. *Phys. Z.* **1923**, 24 (185–206), 1.
- (70) McQuarrie, D. A. Statistical Mechanics; Sterling Publishing Company: 2000.
- (71) Lytle, T. K.; Sing, C. E. Transfer matrix theory of polymer complex coacervation. *Soft Matter* **2017**, *13* (39), 7001–7012.
- (72) Lytle, T. K.; Sing, C. E. Tuning chain interaction entropy in complex coacervation using polymer stiffness, architecture, and salt valency. *Mol. Syst. Des. Eng.* **2018**, 3 (1), 183–196.
- (73) Madinya, J. J.; Chang, L.-W.; Perry, S. L.; Sing, C. E. Sequence-dependent self-coacervation in high charge-density polyampholytes. *Mol. Syst. Des. Eng.* **2020**, *5* (3), 632–644.
- (74) Ong, G. M. C.; Sing, C. E. Mapping the phase behavior of coacervate-driven self-assembly in diblock copolyelectrolytes. *Soft Matter* **2019**, *15* (25), 5116–5127.
- (75) Bevensee, M. O.; Boron, W. F. Control of Intracellular pH. In Seldin and Giebisch's The Kidney, 4th ed.; Alpern, R. J., Hebert, S. C., Eds.; Academic Press: San Diego, 2008; Chapter 51, pp 1429–1480.
- (76) Heller, W.; Pangonis, W. J. Theoretical Investigations on the Light Scattering of Colloidal Spheres. I. The Specific Turbidity. *J. Chem. Phys.* **1957**, 26 (3), 498–506.
- (77) Cutillas, S.; Meunier, A.; Lemaire, E.; Bossis, G.; Persello, J. Phase Separation and Turbidity of Electrorheological Fluids. *Int. J. Mod. Phys. B* **1996**, *10* (23n24), 3093–3101.
- (78) Han, J. Y.; Burgess, K. Fluorescent Indicators for Intracellular pH. Chem. Rev. **2010**, 110 (5), 2709–2728.
- (79) Fu, K.; Pack, D. W.; Klibanov, A. M.; Langer, R. Visual evidence of acidic environment within degrading poly(lactic-coglycolic acid) (PLGA) microspheres. *Pharm. Res.* **2000**, *17* (1), 100–106.
- (80) Zhang, F.; Ali, Z.; Amin, F.; Feltz, A.; Oheim, M.; Parak, W. J. Ion and pH Sensing with Colloidal Nanoparticles: Influence of

- Surface Charge on Sensing and Colloidal Properties. ChemPhysChem 2010, 11 (3), 730-735.
- (81) Huang, D.; Zhao, T.; Xu, W.; Yang, T.; Cremer, P. S. Sensing Small Molecule Interactions with Lipid Membranes by Local pH Modulation. *Anal. Chem.* **2013**, *85* (21), 10240–10248.
- (82) Jung, H.; Robison, A. D.; Cremer, P. S. Detecting Protein-Ligand Binding on Supported Bilayers by Local pH Modulation. *J. Am. Chem. Soc.* **2009**, *131* (3), 1006–1014.
- (83) Sekine, Y.; Houston, R.; Sekine, S. Cellular metabolic stress responses via organelles. *Exp. Cell Res.* **2021**, 400 (1), 112515.
- (84) Klein, I. A.; et al. Partitioning of cancer therapeutics in nuclear condensates. *Science* **2020**, *368* (6497), 1386–1392.
- (85) Hong, K.; Song, D.; Jung, Y. Behavior control of membrane-less protein liquid condensates with metal ion-induced phase separation. *Nat. Commun.* **2020**, *11* (1), 5554.